

Superior Durability of Dissimilar Material Joint between Steel and Thermoplastic Resin with Roughened Electrodeposited Nickel Interlayer

Susumu Arai,* Ryo Sugawara, Masahiro Shimizu, Junki Inoue, Masaomi Horita, Takashi Nagaoka, and Masami Itabashi

The durability of the dissimilar material joint between a steel coated with a roughened nickel plating-film and a thermoplastic resin is assessed. The roughened nickel film is fabricated by electrodeposition using carbon nanotubes (CNTs) as the roughening agent and a polyphenylenesulfide (PPS) resin as the thermoplastic resin. The plated steel and PPS resin are joined by injection molding without adhesive. The bonding strength is determined by a tensile lap shear strength test during the durability tests that includes a high-temperature and high-humidity test ($85 \pm 2^\circ\text{C}$, $85 \pm 2\%$ relative humidity; 0–2000 h) and a thermal shock test (-50°C – 150°C ; 0–1000 cycles). During the high-temperature and high-humidity test, the bonding samples maintain their initial bonding strength (>40 MPa) even after 2000 h. By contrast, during the thermal shock test, although the bonding strength gradually decreases with increasing number of cycles, it remains above 20 MPa even after 1000 cycles. The mechanism of the deterioration of the bonding strength during the thermal shock test is analyzed in detail. The present joining method, which uses a roughened plating film as an interlayer, offers a way to achieve not only high initial bonding strength but also bonding durability for dissimilar material joining between steels and resins.

helps to mitigate global warming.^[1] “Multimaterialization,” technologies for joining dissimilar materials are very important.^[2] In particular, a technology for joining steel and fiber-reinforced plastics is not only effective for reducing the weight of cars, but also suitable for producing widely acceptable inexpensive cars. This is because steel, although heavy, has been used mainly for car frames due to its excellent mechanical properties and low price, and fiber-reinforced plastics, including carbon-fiber-reinforced plastics, are lightweight and have superior mechanical properties.

Recently, the joining of metals and thermoplastic resins by applying a thermoplastic resin onto a roughened metal surface has attracted great attention. The bonding strength of this joint derives mainly from the so-called “anchor effect.” Generally, the resin is applied by injection molding or hot pressing, which forces the plastic into irregularities on the metal surface. A roughened metal surface is essential to achieve a strong anchor effect,

and hence strong bonding. Laser treatment,^[3–9] chemical etching,^[10,11] and abrasive blasting,^[12–14] are effective methods for roughening a metal surface. However, in the case of these methods, the morphology of the roughened surface, and the resulting bonding strength, differ for each metal and alloy. Thus, a new method has been sought to create the same roughened surface morphology regardless of the type of metal or alloy. Plating is thought to offer the same surface morphology regardless of the substrate, because the surface morphology of the plating depends on the plating conditions, not on the substrate. Our research group has reported that a strong bond can be obtained between steel and a thermoplastic resin through a roughened plating technique using carbon nanotubes (CNTs).^[15] In practice, to achieve this technology, the bonding durability must be characterized.


In this work, steel and a thermoplastic resin were joined by using an electrodeposited roughened nickel film as the interlayer, and the shear strengths of the bonding samples were measured during both a high-temperature and high-humidity test and a thermal shock test. Furthermore, the microstructures of the joints during the tests, in particular, the thermal shock test, were examined in detail.

1. Introduction

Combining multiple materials is effective for reducing the weight of vehicles, such as cars, which reduces CO₂ emissions and

Prof. S. Arai, R. Sugawara, Dr. M. Shimizu, J. Inoue, Dr. M. Horita
Department of Materials Chemistry
Faculty of Engineering
Shinshu University
4-17-1 Wakasato, Nagano 380-8553, Japan
E-mail: araisun@shinshu-u.ac.jp

T. Nagaoka, M. Itabashi
Taisei Plas Co., Ltd.
1-10-5 Honcho, Nihonbashi, Chuo, Tokyo 103-0023, Japan

 The ORCID identification number(s) for the author(s) of this article can be found under <https://doi.org/10.1002/adem.202000739>.

© 2020 The Authors. Published by Wiley-VCH GmbH. This is an open access article under the terms of the Creative Commons Attribution License, which permits use, distribution and reproduction in any medium, provided the original work is properly cited.

DOI: 10.1002/adem.202000739

2. Experimental Section

A plating bath consisting of 250 g $\text{NiSO}_4 \cdot 6\text{H}_2\text{O}$, 45 g L^{-1} $\text{NiCl}_2 \cdot 6\text{H}_2\text{O}$, 20 g L^{-1} $\text{C}_6\text{H}_5\text{Na}_3\text{O}_7$ (citric acid), 2 g L^{-1} CNTs, and 0.1 g L^{-1} polyacrylic acid was used for preparing Ni/CNT composite films. The commercially available multiwalled CNTs (VGCF, Showa Denko Co. Ltd.) used were 100–150 nm in diameter and 10 μm in length. Polyacrylic acid (PAA, mean molecular weight: 5000) was utilized as the CNT dispersant.^[16–18] The substrate was a cold-rolled steel sheet (SPCC, JIS G 3141), measuring $1.8 \times 4.5 \times 0.15 \text{ cm}^3$ in size, that was coated with an insulating tape to expose a cathode area of 1.8 cm^2 ($1.8 \times 1.0 \text{ cm}^2$). A pure nickel plate was used as the anode. A commercially available electrolytic cell (Microcell model I, Yamamoto-Ms Co., Ltd.) was used for the electrodeposition. Electrodeposition was carried out under galvanostatic conditions (10 mA cm^{-2}) at room temperature ($\approx 25^\circ\text{C}$) with aeration. The electrical charge was 29.3 C cm^{-2} . The Ni/CNT composite film obtained was chemically etched with 20 wt% HNO_3 at 50°C for 30 s and then ultrasonicated for 60 s in pure water using an ultrasonic cleaner (VS-100 As-One) to remove the CNTs that adhered to the etched surface. The CNTs generated a micrometer-order undulation on the Ni/CNT composite film by being captured into the deposited Ni during the composite plating. In addition, the CNTs left submicrometer-order traces after being removed from the surface of the Ni/CNT composite film during the etching and ultrasonication processes. **Figure 1a** shows the surface scanning electron microscopy (SEM) image of a roughened nickel film on a SPCC substrate after the etching process.^[15] In addition to the microscopic undulation due to the incorporation of the CNTs in the deposited nickel,^[19] the traces of CNTs (submicrometer order) and anisotropic etching marks of the deposited nickel (tens of nanometers), caused by etching and ultrasonication, are visible on the surface. The combination of these three scales of roughness (i.e., micrometer, submicrometer, and tens

of nanometers) is presumably what generates a strong anchor effect (triple anchor effect).^[15]

Polyphenylenesulfide (PPS, SGX-120 [containing 20 mass% glass fibers] TOSOH Co., Ltd.) was used as the thermoplastic resin. Bonding samples were formed using an injection molding machine (PNX60, Nissei Plastic Industrial Co., Ltd.). The initial temperature of the PPS resin was 310°C , and the mold was maintained at 140°C . The injection pressure was 136 MPa. A photograph and the dimensions of the bonding sample are shown in **Figure 1b**. The sample size conforms to ISO 19095.^[20] The bonding area between the plated SPCC substrate and the PPS resin plate was 0.5 cm^2 ($1.0 \times 0.5 \text{ cm}^2$).

The high-temperature and high-humidity test was carried out using a constant temperature and humidity tester (IH4000; Yamato Science Co. Ltd.). The temperature was $85 \pm 2^\circ\text{C}$, and the relative humidity was $85 \pm 2\%$. The testing times were 24, 48, 168, 336, 672, 1000, 1500, and 2000 h. These conditions conform to ISO 19095.^[20] The number of samples was 3 ($n = 3$).

The thermal shock test was conducted using a thermal shock tester (TSE-11; Espec Corp.). The low and high temperatures were -50 and 150°C , respectively. The number of testing cycles was 10, 50, 100, 200, 500, and 1000. These conditions almost conform to ISO 19095,^[20] however, the temperature range was more severe than the most severe condition regulated in ISO 19095 (-40 to 150°C). Thus, the temperature condition used in this study was extremely harsh. The number of samples was 5 ($n = 5$). The thermal shock test pattern is shown in **Figure 1c**. Bonding strength during durability testing was evaluated by a tensile lap shear strength test, as described in ISO 19095^[20] using a universal testing machine (AGS-J 10 kN; Shimadzu Seisakusho Co. Ltd.). The load range and sensor accuracy of the testing machine were 10 kN and $\pm 0.1\%$, respectively. The test was conducted at a constant crosshead speed (10 mm min^{-1}). A photograph of a specimen retainer for the test is shown in **Figure 1d**.

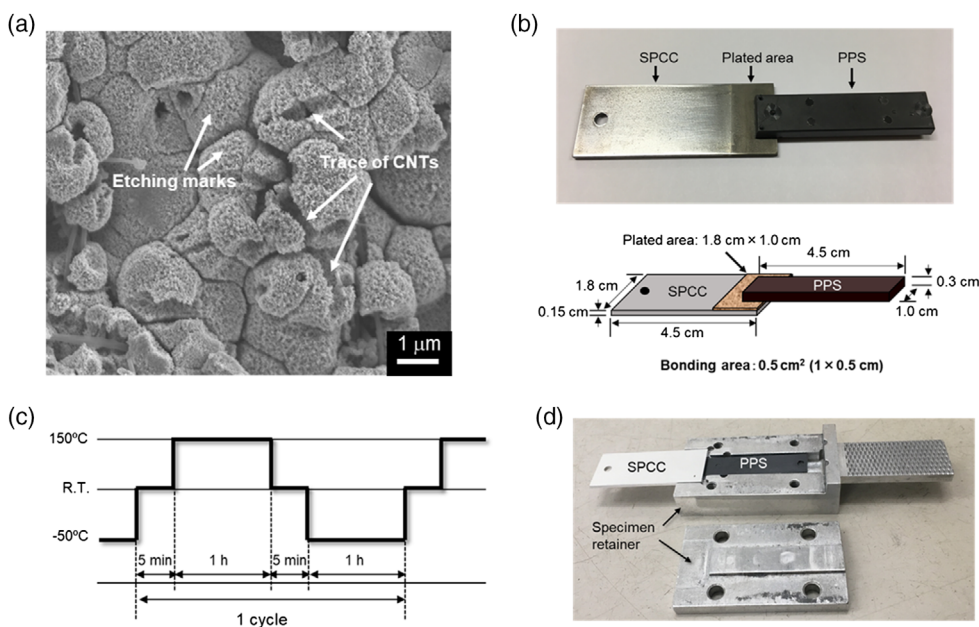


Figure 1. a) Surface SEM image of roughened nickel film after chemical etching. b) Photograph and dimensions of bonding sample. c) Thermal shock test pattern. d) Photograph of the jig for the tensile lap shear strength test.

The fracture surfaces after the tensile lap shear strength test were imaged by field-emission scanning electron microscopy (FE-SEM, 7000F JEOL Ltd.), and the cross-sectional FE-SEM image and energy-dispersive X-ray spectroscopy (EDS) mapping image of the bonding samples were analyzed by focused ion beam FE-SEM (JIB-4610F JEOL Ltd.). Nondestructive analysis of the nonshear-tested bonding samples during the thermal shock test was conducted using a scanning acoustic tomograph (SAT, FineSAT V Hitachi Power Solutions Co. Ltd.).

3. Results and Discussion

3.1. Durability against High-Temperature and High-Humidity Test

3.1.1. Shear Strength

During the high-temperature and high-humidity test, while red iron rust was detected on the unplated area of the SPCC substrate, no red iron rust was observed on the unjoined nickel-plated area of the SPCC substrate. **Figure 2** shows the variation in the shear strength during the high-temperature and high-humidity test. The shear strength was almost unchanged during the test, remaining above 40 MPa even after 2000 h.

Furthermore, the variation was insignificant. Thus, the durability of the bond between the SPCC and PPS resin with the roughened electrodeposited nickel interlayer against high temperature and high humidity was excellent.

3.1.2. Fracture Surface

Figure 3 shows the fracture surfaces of the bonding samples before and after the high-temperature and high-humidity test (2000 h). **Figure 3a,b** shows the fracture surfaces in the bonding area of both the PPS resin side and the SPCC side (roughened nickel film on SPCC) before and after the test, respectively. On both surfaces of the PPS resin side and the SPCC side before and after the test, cohesive failure of the PPS resin was clearly seen by

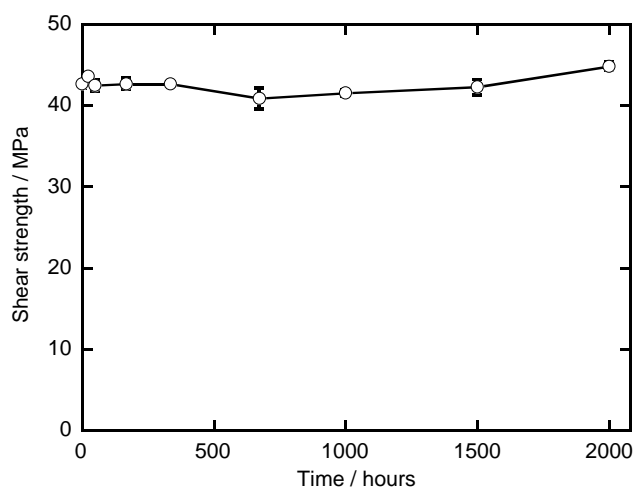


Figure 2. Variation in shear strength during the high-temperature and high-humidity test.

visual inspection. To determine whether any fracture modes other than cohesive failure occurred at the microscopic level, the PPS resin was examined by SEM. **Figure 3c,d** shows the SEM fractographs of points A and B in **Figure 3a**, whereas **Figure 3e,f** shows the SEM fractographs of points C and D in **Figure 3b**, respectively. The PPS resin exhibited uniform fracture morphologies on all surfaces of points A, B, C, and D, respectively. Thus, the fracture mode was cohesive failure of the PPS resin at the microscopic scale before and after the high-temperature and high-humidity test.

These results also showed that both the material strength of the roughened nickel film and the bonding strength between the roughened nickel film and the SPCC substrate must be higher than the material strength of the PPS resin during the high-temperature and high-humidity test.

3.1.3. Microstructure of Boundary between Roughened Nickel and Resin

Figure 4 shows cross-sectional SEM images of the boundary between the SPCC substrate and the PPS resin before and after the high-temperature and high-humidity test (2000 h). A comparison shown in **Figure 4a,b** reveals that no significant shape change is seen due to the test (**Figure 4b**). Thus, although red iron rust was observed on the bare area of the SPCC substrate, no corrosion was seen on the SPCC substrate on either the unjoined nickel-plated area of the SPCC substrate or at the boundary between the SPCC substrate and the PPS resin even after the 2000 h high-temperature and high-humidity test. These results are presumably due to the corrosion resistance of the roughened nickel film. During the high-temperature and high-humidity test, as nickel has a higher standard electrode potential than iron ($\text{Ni}^{2+} + 2\text{e}^- \rightarrow \text{Ni}$; $E^0 = -0.23 \text{ V}$ vs standard hydrogen electrode, $\text{Fe}^{2+} + 2\text{e}^- \rightarrow \text{Fe}$; $E^0 = -0.44 \text{ V}$ vs standard hydrogen electrode) and it forms a passive film in air, the roughened nickel film must protect the SPCC substrate against corrosion. Furthermore, there is concern that during the high-temperature and high-humidity test, moisture gradually penetrates the boundary between the SPCC substrate (the roughened-nickel-plated SPCC) and the PPS resin,^[21] thus causing corrosion of the SPCC substrate. However, as the roughened nickel film has a large surface area, which means that the distance along the interface of the roughened nickel layer and the PPS resin is considerably long, moisture cannot easily enter from the surface and penetrate the boundary between the roughened nickel layer and the PPS resin. For these reasons, no corrosion occurred at the boundary between the SPCC substrate and the PPS resin or in the unjoined nickel-plated area of the SPCC during the high-temperature and high-humidity test, resulting in excellent bonding durability (**Figure 2**).

3.2. Durability against Thermal Shock Test

3.2.1. Shear Strength

Figure 5 shows the variation in shear strength during the heat shock test. The shear strength did decrease gradually; however, the variation at each cycle number was small: the shear strength

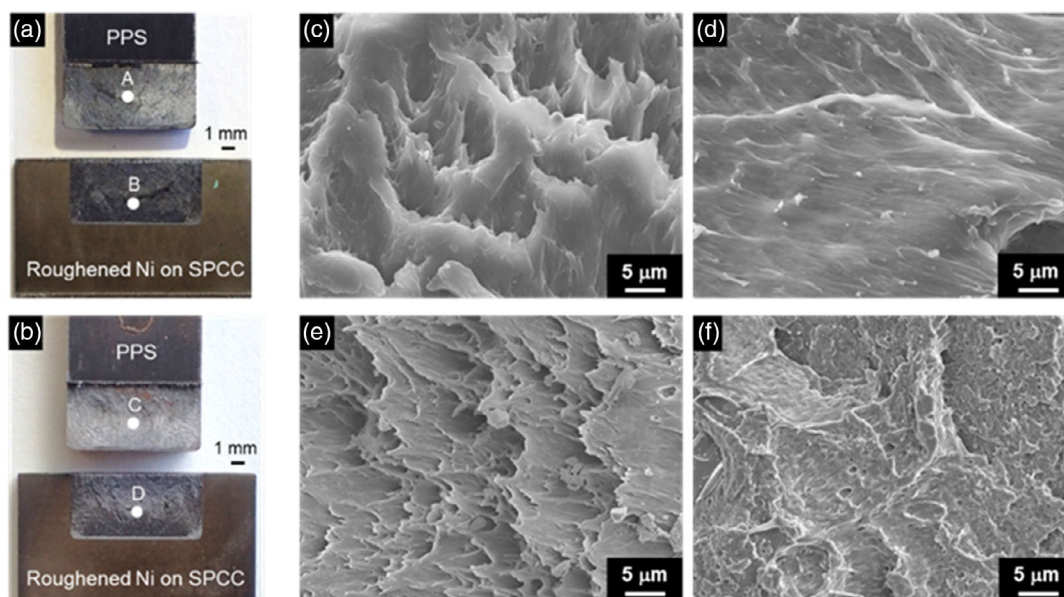


Figure 3. Fracture surfaces of the bonding samples before and after the high-temperature and high-humidity test (2000 h). a) Photograph of fracture surface before the test, b) photograph of fracture surface after the test, c) surface SEM image of point A in (a), d) surface SEM image of point B in (a), e) surface SEM image of point C in (b), and f) surface SEM image of point D in (b).

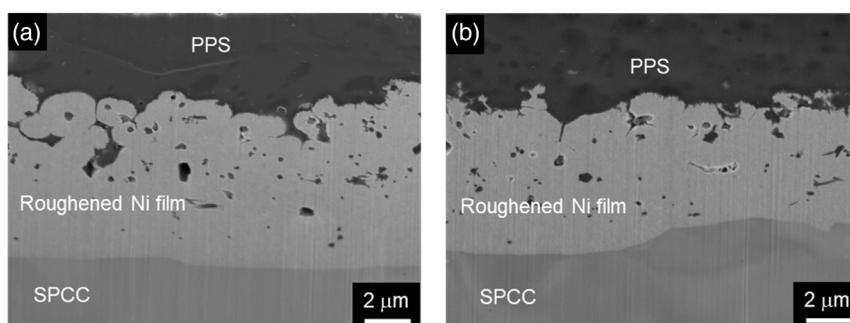


Figure 4. Cross-sectional SEM images of the boundary between SPCC substrate and PPS substrate a) before and b) after the high-temperature and high-humidity test (2000 h).

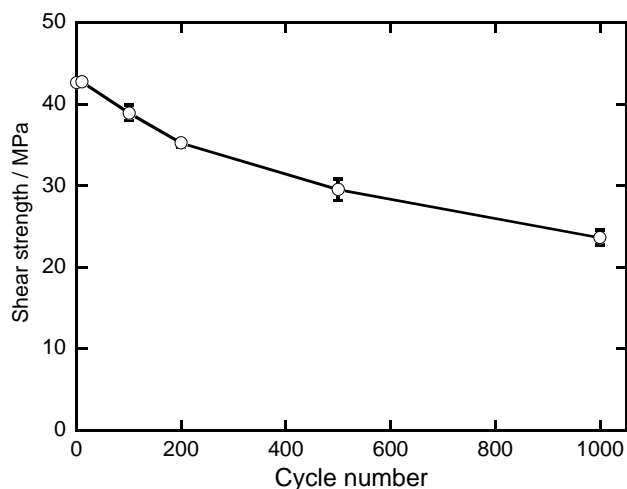


Figure 5. Variation in shear strength during heat shock test.

was over 20 MPa even after 1000 cycles. Considering the severe temperature condition (-50 to 150 °C), the bond between the SPCC substrate and the PPS resin with a roughened electrodeposited nickel interlayer has high durability against the heat shock test.

3.2.2. Fracture Surface

The fracture surfaces of the bonding samples used in the heat shock test are shown in **Figure 6**. Visual inspection reveals two morphologies after the test (Figure 6b–d) that clearly differ from the fracture surfaces before the test, which exhibit a uniform morphology over the entire surface (Figure 6a). In addition to bright central regions, which exhibit nearly the same morphology as that before the test (Figure 6a), dark regions are seen at the edges. These dark regions spread toward the center of the bonding area with increasing cycle number (Figure 6b–d). Figure 6e–h shows surface SEM images of the fracture surfaces shown in Figure 6d.

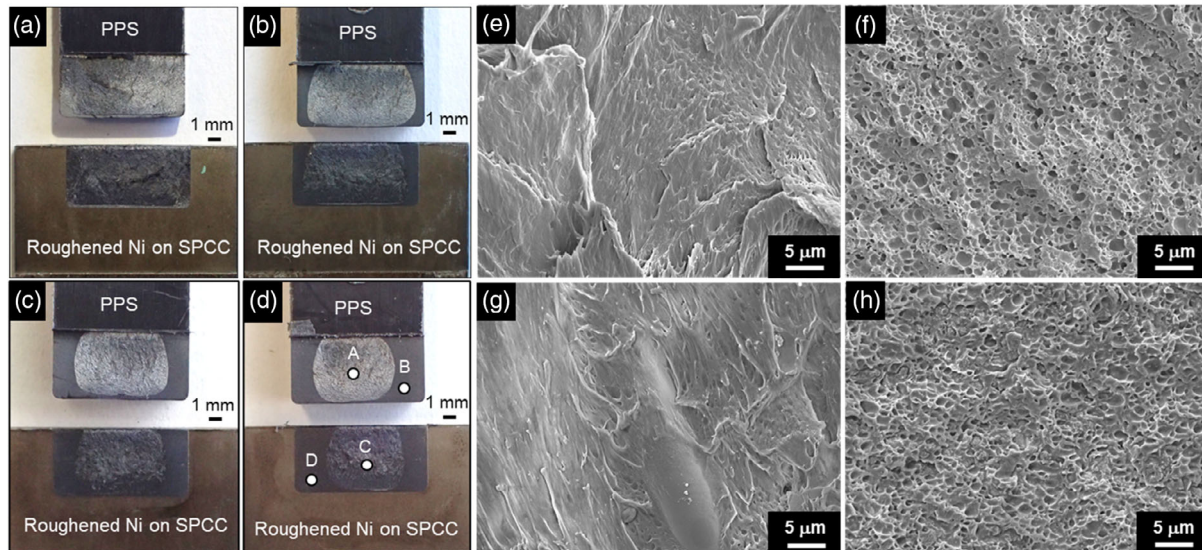


Figure 6. Fracture surfaces of the bonding samples before and after the heat shock testing. a) Photograph of the fracture surface before the test. b–d) Photographs of fracture surfaces after 200, 500, and 1000 cycles, respectively. e–h) SEM images at points A, B, C, and D in (d), respectively.

Figure 6e,f shows SEM images of points A (central region of PPS side) and B (edge of PPS side) in Figure 6d, respectively. Figure 6g,h shows SEM images of points C (central region of SPCC side) and D (edge of SPCC side) in Figure 6d, respectively. Morphologies similar to that before the test (Figure 3c) are seen at points A (Figure 6e) and C (Figure 6g). In contrast, many voids are observed on the fracture surfaces at points B (Figure 6f) and D (Figure 6h); similar SEM images were obtained for the fracture surfaces after thermal shock tests of 200 and 500 cycles, respectively. It remains unclear why the voids formed. Thus, the fracture mode in the central regions must be cohesive failure of the PPS resin. A different fracture mode was observed at the edges.

3.2.3. Microstructure of Boundary between Roughened Nickel and Resin

To identify the fracture mechanism in the edge regions, a non-destructive analysis was conducted at the boundaries of the non-shear-tested bonding samples during the thermal shock test. **Figure 7** shows SAT images of the bonding areas of the

nonshear-tested bonding samples taken during the thermal shock test. The fracture surfaces (PPS sides in Figure 6a–d), as observed during the thermal shock test, are also shown for comparison. Before the thermal shock test, the SAT image is uniformly gray (Figure 7a), which means that no significant gaps exist at the boundary of the SPCC substrate and the PPS resin. SAT images obtained after the thermal shock test show bright regions at the edges, in addition to the central gray region and the bright region spreading toward the center of the bonding area with increasing cycle number (Figure 7b–d). These bright regions indicate that gaps exist around the boundaries of the bonding area. Photographs of the fracture surfaces obtained during the thermal shock test (Figure 7e–h) closely resemble their SAT images.

These results indicate that the fractures in the edge regions must be related to the gaps formed during the thermal shock test. To highlight the locations of the gaps, a cross-sectional analysis was conducted in the bright and dark areas in the SAT images (Figure 7b–d).

Figure 8 shows cross-sectional SEM images and the results of EDS mapping of the nonshear-tested bonding samples used in the thermal shock test. The SAT images (Figure 8a–c) indicate

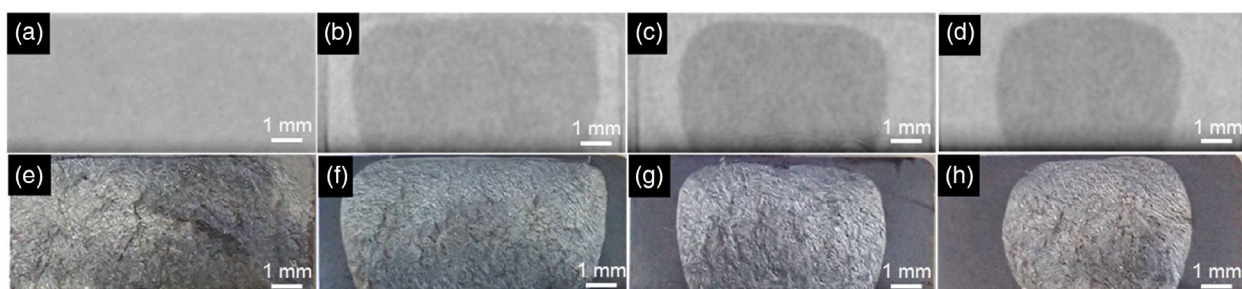


Figure 7. SAT images of nonshear-tested bonding samples and photographs of shear-tested bonding samples (PPS side). a) SAT image before the test; b–d) SAT images after 200, 500, and 1000 cycles, respectively; e) Photograph of the fracture surface before the test; f–h) Photographs of fracture surfaces after 200, 500, and 1000 cycles, respectively.

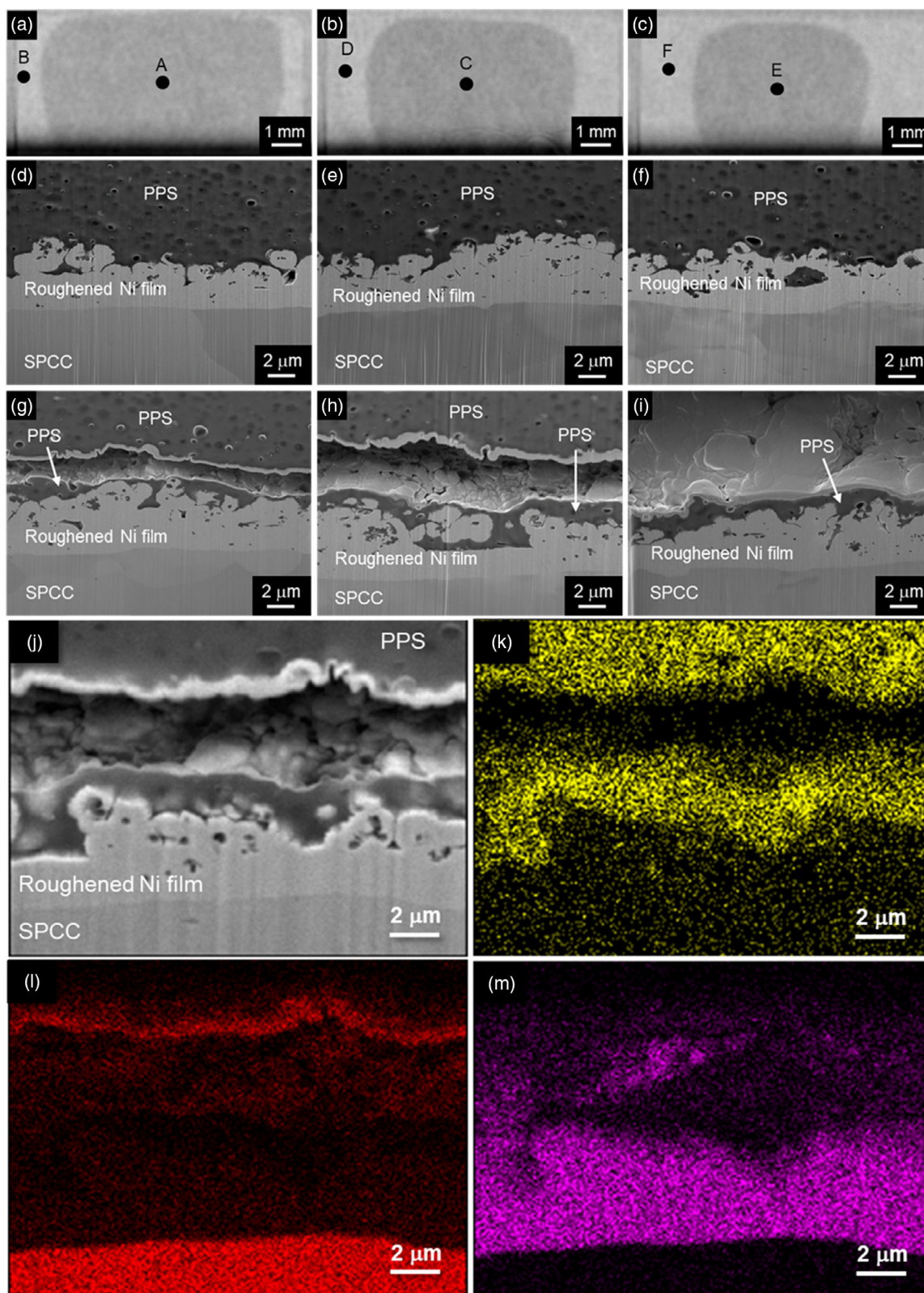


Figure 8. Cross-sectional SEM images and the results of EDS mapping of the boundaries of the nonshear-tested bonding samples after the thermal shock test. a–c) SAT images of bonding samples after thermal shock tests of 200, 500, and 1000 cycles, respectively. Points A–F in the SAT images are cross-sectional analysis points. d–i) Cross-sectional SEM images of points A–F, respectively. j) Cross-sectional SEM image of bonding sample after thermal shock test of 500 cycles. k–m) Elemental distributions of C, Fe, and Ni, respectively.

the cross-sectional analysis points. Points A, C, and E are the gray areas in the SAT images; the corresponding cross-sectional SEM images are shown in Figure 8d–f, respectively. These SEM images reveal that no significant morphological changes have occurred during the thermal shock test. Thus, the dark regions (the central region) in the SAT images are the bonding areas where the initial boundary structures between the SPCC substrate and the PPS resin were maintained even after the thermal shock test. By contrast, at the indicated points in the bright regions (B in Figure 8a, D in Figure 8b, and F in Figure 8c), there are evident continuous gaps around the boundaries (Figure 8g–i). The height of the gaps increased with increasing cycle number. In these SEM images, bright film-like areas, which appear like the roughened nickel films, are seen in the upper parts of the gaps (Figure 8g,h). Figure 8j shows the results of EDS mapping analysis at the boundary between the SPCC substrate and the PPS resin after the thermal shock test of 500 cycles (Figure 8h). The distribution of iron indicates that the bright film-like areas consist of iron (Figure 8l). These areas presumably formed from splatter of the iron cluster when the sample including SPCC was etched by the argon beam during FIB processing. The carbon distribution suggests the presence of gaps in the PPS resin (Figure 8k). Nickel is detected in the gap area as well as in the roughened nickel film area (Figure 8m). The nickel in the gap area presumably derives from the roughened nickel film just below the PPS resin.

Thus, a continuous gap was formed in the PPS resin near the roughened nickel film before the shear test during the thermal shock test, and the gap progressed gradually from the edge of the bonding area with increasing cycle number. It is known that stress develops near the edge of the interface of bonded dissimilar materials due to the difference in coefficient of thermal expansion (CTE) between the materials.^[22,23] In this study, steel (SPCC) and PPS resin were joined by a roughened nickel film used as an interlayer. The coefficients of thermal expansion of steel ($1.1 \times 10^{-5} \text{ K}^{-1}$) and PPS resin ($\approx 5 \times 10^{-5} \text{ K}^{-1}$) differ greatly. Although the exact CTE of the roughened nickel film was unknown, the CTE of nickel is $1.3 \times 10^{-5} \text{ K}^{-1}$, which is close to that of steel (SPCC). Therefore, during the thermal shock test, which had a particularly severe temperature condition (-50 to 150°C), a high stress presumably developed at the edge of the interface between the roughened nickel film and the PPS resin, resulting in the formation of cracks in the PPS resin near the nickel film starting from the edge of the bonding area. The SEM images of the dark region of the fracture surface (Figure 6f,h) reveal the surface morphologies of the gaps formed during the thermal shock test. These SEM images also indicate that the bonding strength between the roughened nickel film and the PPS resin, the material strength of the roughened nickel film, and the bonding strength between the roughened nickel film and the SPCC substrate exceeded the material strength of the PPS resin throughout the thermal shock test.

The shear strength of the bonding samples deteriorated during the thermal shock test as the bonding area decreased due to the formation of gaps in the PPS resin near the roughened nickel interlayer. The formation of gaps is attributable to the difference in CTE between the nickel film (and/or SPCC substrate) and the PPS resin. Thus, improvement of the material strength of the PPS resin and relaxation of the difference in CTE between the roughened plating film and the PPS resin

are thought to be effective in improving bonding durability during thermal shock testing.

4. Conclusion

Superior bonding durability between the steel and resin was achieved using a roughened electrodeposited nickel film as an interlayer. The shear strength maintained its high initial value of over 40 MPa during the high-temperature and high-humidity test ($85 \pm 2^\circ\text{C}$, $85 \pm 2\%$ RH) even after 2000 h, and no structural change was observed at the boundary after the test. During the thermal shock test (-50 to 150°C), although the shear strength decreased gradually, it remained over 20 MPa even after 1000 cycles. The deterioration in bonding strength was mainly caused by the degradation in the resin near the roughened nickel interlayer. No degradation in the nickel interlayer or exfoliation of the interlayer from the steel was observed.

Acknowledgements

The authors thank Yousei Sakaigawa and Kaoru Onodera of Hitachi Power Solutions Co. Ltd. for performing the SAT analysis. This research was supported by the Japan Science and Technology Agency (JST), Adaptable and Seamless Technology transfer Program through Target-driven R&D (A-STEP: Grant No. JPMJTM19B9).

Conflict of Interest

The authors declare no conflict of interest.

Keywords

anchor effects, bonding durabilities, multimaterialization, roughened nickel-plating films, steel-resin joinings

Received: June 19, 2020

Revised: July 23, 2020

Published online: September 6, 2020

- [1] M. Goede, M. Stehlin, L. Rafflenbeul, G. Kopp, E. Beeh, *Eur. Trans. Res. Rev.* **2009**, 1, 5.
- [2] S. T. Amancio-Filho, J. F. dos Santos, *Polym. Eng. Sci.* **2009**, 49, 1461.
- [3] M. Seto, Y. Asami, M. Itakura, H. Tanaka, M. Yamabe, *J. Jpn. Soc. Polym. Process* **2015**, 27, 68.
- [4] K. Taki, S. Nakamura, T. Takayama, A. Nemoto, H. Ito, *Microsyst. Technol.* **2016**, 22, 31.
- [5] P. A. Fabrin, M. E. Hoikkanen, J. E. Vuorinen, *Polym. Eng. Sci.* **2007**, 47, 1187.
- [6] J. B. Nielsen, J. V. Boll, A. H. Holm, R. Hojsholt, P. Balling, *Int. J. Adhes. Adhes.* **2010**, 30, 485.
- [7] A. Roesner, S. Scheik, A. Olowinsky, A. Gillner, U. Reisgen, M. Schleser, *Phys. Procedia* **2011**, 12, 370.
- [8] P. Amend, S. Pfindel, M. Schmidt, *Phys. Procedia* **2013**, 41, 98.
- [9] Y. Kurakake, Y. Farazila, Y. Miyashita, Y. Otsuka, Y. Mutoh, *J. Laser Micro/Nanoeng.* **2013**, 8, 161.
- [10] W. S. Kim, I. H. Yun, J. J. Lee, H. T. Jung, *Int. J. Adhes. Adhes.* **2010**, 30, 408.
- [11] F. Kimura, S. Kadoya, Y. Kajihara, *Precis. Eng.* **2016**, 45, 203.

- [12] K. Ramani, B. Moriarty, *Polym. Eng. Sci.* **1998**, 35, 870.
[13] A. F. Harris, A. Beevers, *Int. J. Adhes. Adhes.* **1999**, 19, 445.
[14] G. Lucchetta, F. Marinello, P. F. Bariani, *CIRP Ann. Manuf. Technol.* **2011**, 60, 559.
[15] S. Arai, R. Sugawara, M. Shimizu, J. Inoue, M. Horita, T. Nagaoka, M. Itabashi, *Mater. Lett.* **2020**, 263, 127241.
[16] S. Arai, M. Endo, *Electrochem. Commun.* **2003**, 5, 797.
[17] S. Arai, S. Takashi, M. Endo, *J. Electrochem. Soc.* **2007**, 154, D530.
[18] S. Arai, F. Akihiro, M. Masami, M. Endo, *Mater. Lett.* **2008**, 62, 3545.
[19] S. Arai, M. Endo, N. Kaneko, *Carbon* **2004**, 42, 641.
[20] British Standards Institution, *Plastics-Evaluation of the Adhesion Interface Performance in Plastic-Metal Assemblies – Part 3: Test Methods*, ISO 19095-3, British Standards Institution, London **2015**.
[21] R. Iwasaki, C. Sato, H. Yamabe, *J. Adhesion Soc. Jpn.* **2007**, 43, 81.
[22] D. Munz, Y. Y. Yang, *Int. J. Fracture* **1993**, 60, 169.
[23] Y. Y. Yang, D. Munz, *Int. J. Solid Struct.* **1997**, 34, 1199.